RSC Advances

ROYAL SOCIETY OF CHEMISTRY

PAPER

View Article Online
View Journal | View Issue

Check for updates

Cite this: *RSC Adv.*, 2018, **8**, 25514

A vertical WSe_2–$MoSe_2$ p–n heterostructure with tunable gate rectification†

Hailing Liu, ‡[ab] Sajjad Hussain,‡[ab] Asif Ali,[ab] Bilal Abbas Naqvi,[ab] Dhanasekaran Vikraman, [c] Woonyoung Jeong,[ab] Wooseok Song, [d] Ki-Seok An [d] and Jongwan Jung *[ab]

Received 20th April 2018
Accepted 4th July 2018

DOI: 10.1039/c8ra03398f

rsc.li/rsc-advances

Here, we report the synthesis of a vertical $MoSe_2/WSe_2$ p–n heterostructure using a sputtering-CVD method. Unlike the conventional CVD method, this method produced a continuous $MoSe_2/WSe_2$ p–n heterostructure. WSe_2 and $MoSe_2$ back-gated field effect transistors (FETs) exhibited good gate modulation behavior, and high hole and electron mobilities of ~2.2 and ~15.1 $cm^2\ V^{-1}\ s^{-1}$, respectively. The fabricated vertical $MoSe_2/WSe_2$ p–n diode showed rectifying *I–V* behavior with back-gate tunability. The rectification ratio of the diode was increased with increasing gate voltage, and was increased from ~18 to ~1600 as the gate bias increased from −40 V to +40 V. This is attributed to the fact that the barrier height between p-WSe_2 and n-$MoSe_2$ is modulated due to the back-gate bias. The rectification ratio is higher than the previously reported values for the TMDC p–n heterostructure grown by CVD.

1. Introduction

The two-dimensional transition metal dichalcogenides (TMDCs), in the form of MX_2 (M = metal and X = S, Se or Te), have recently received much attention for the study of physics in 2D materials and in layered structures.[1–3] In TMDCs, each M-atom (transition metal element) layer is enclosed within two X-atom (chalcogen element) layers and the atoms in the layers have hexagonally packed structures.[1,3,4] Every X–M–X atom arrangement is held together by van der Waals interactions. And due to the weak van der Waals interactions of each layer, it is possible to tune the band structure of the X–M–X atoms from an indirect (~1.2 eV) to a direct band gap (~2.5 eV) through heterogeneous integration. TMDCs exhibit good electrical properties[1,3,5,6] with high on/off ratios of ~10^8, and room-temperature mobility over 200 $cm^2\ V^{-1}\ s^{-1}$.[7–11] Due to weak van der Waals forces between each stacking layer, 2D heterostructures can be easily produced by using mechanical transfer methods. Since p–n junctions are basic building blocks for electronic devices, and other optoelectronic devices,[12–14] the implementation of homo or hetero p–n junctions is a key interest among researchers. Mechanical exfoliation is an easy way to produce p–n junctions; however, it is not suitable for mass production. Recently, many efforts have been made to apply chemical vapor deposition (CVD) to 2D heterostructures such as MoS_2/graphene,[15] WS_2/MoS_2,[16] WS_2/h-BN,[17] and n-MoS_2/p-WSe_2,[18] $MoSe_2$–WSe_2.[18] Nonetheless, the current rectification behavior of CVD-grown TMDC heterostructures is rarely reported and is poor.[18] Our group has been focusing on the synthesis of TMDCs by a sputtering-CVD method.[19,20] In this paper, we report a $MoSe_2/WSe_2$ p–n heterostructure. A W film was sputtered and then selenized to form WSe_2, and Mo was sputtered on the WSe_2 and selenized to form a vertical $MoSe_2$ (n)/WSe_2 (p) junction. Unlike the conventional CVD method, this method produces a continuous $MoSe_2/WSe_2$ film. The WSe_2 and $MoSe_2$ back-gate field effect transistors (FETs) exhibited good gate modulation behavior, and high hole and electron mobilities of ~2.2 and ~15.1 $cm^2\ V^{-1}\ s^{-1}$, respectively. The fabricated $MoSe_2/WSe_2$ p–n diodes showed rectifying *I–V* behavior, and the forward diode current increased with increasing back-gate bias. The p–n diode with back-gate tunability showed a high gate-tunable rectification ratio varying from ~18 to ~1600 at different back-gate biases. This can be attributed to the fact that the barrier height between p-WSe_2 and n-$MoSe_2$ is modulated due to the back-gate bias. The rectification ratio is much higher than the previously reported value for the TMDC p–n heterostructure (MoS_2/WSe_2) grown by CVD.[18]

[a] *Graphene Research Institute, Sejong University, Seoul 143-747, Republic of Korea. E-mail: jwjung@sejong.ac.kr*

[b] *Institute of Nano and Advanced Materials Engineering, Sejong University, Seoul 143-747, Republic of Korea*

[c] *Division of Electronics and Electrical Engineering, Dongguk University-Seoul, Seoul 04620, Republic of Korea*

[d] *Thin Film Materials Research Center, Korea Research Institute of Chemical Technology, Daejon 305-600, Korea*

† Electronic supplementary information (ESI) is available. See DOI: 10.1039/c8ra03398f

‡ Authors contributed equally.

2. Experimental details

2.1 Synthesis of $MoSe_2/WSe_2$

Fig. 1 illustrates the overall growth scheme for the vertical $MoSe_2/WSe_2$ heterostructure. The $MoSe_2/WSe_2$ films were

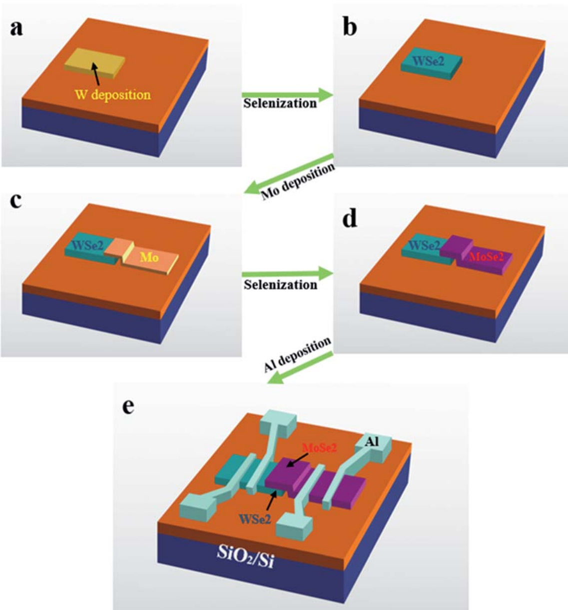

Fig. 1 Schematic of the $MoSe_2/WSe_2$ heterostructure. (a) W was deposited onto the SiO_2/Si substrate. (b) A WSe_2 film was formed *via* selenization. (c) Molybdenum (Mo) was deposited on the top of the WSe_2. (d) A $MoSe_2/WSe_2$ heterostructure was formed *via* selenization. (e) The $MoSe_2/WSe_2$ heterostructure with Al electrodes.

prepared by a RF magnetron sputtering system combined with a selenization process, using a W (99.9% pure) and a Mo (99.9% pure) target in an argon environment at room temperature. Initially a W thin film with a desired thickness was sputtered on a SiO_2/Si substrate through a metal shadow mask. Before sputtering, the chamber was evacuated by a turbomolecular pump to a vacuum at $\sim 2 \times 10^{-6}$ Torr. During the film deposition, the Ar gas was maintained at 10 sccm, and the power was fixed at 150 W with a deposition time of 1200 s. Subsequently, the as-deposited W film was further put in the center of a furnace for selenization at 650 °C for 30 min to form a WSe_2 film. The heating area for the selenium evaporation was fixed at 270 °C. The amount of selenium powder (0.5–0.8 g) used and the flow of Ar as a carrier gas were fixed for all the experiments. After the growth of the WSe_2, a Mo film was deposited on it. The sputtering conditions were the same for both films (W & Mo). The Mo/WSe_2 film was again placed in the tube furnace for selenization annealing to form the $MoSe_2/WSe_2$ heterojunction. The p–n junction area was defined by overlapped regions of two layers (Fig. 1). After the formation of the active area, Al (100 nm) was deposited on the top *via* e-beam evaporation.

2.2 Characterization techniques

All the samples were characterized using the latest analytical characterization techniques. WSe_2, $MoSe_2$ and $MoSe_2/WSe_2$ heterostructure films were analyzed by using a Renishaw inVia RE04, with a 514 nm Ar laser, a laser spot-size of 1 μm, laser power of 10 mW, and an exposure time of 30 s. A Si substrate with a Raman peak of 520 cm^{-1} was used for calibration. X-ray photoelectron spectroscopy (XPS) (PHI 5000 Versa Probe, 25 W Al Kα, 6.7×10^{-8} Pa) was used for binding energy and elemental composition analysis. The crystallinity of the film was examined using in-plan X-ray diffraction (XRD, Rigaku) with Cu-Kα radiation ($\lambda = 54\,178$ Å) operated at 50 kV and 300 mA current. FE-SEM (HITACHI S-4700) was used to demonstrate the morphological nature of the WSe_2, $MoSe_2$ and $MoSe_2/WSe_2$ heterostructure films. The crystal structures of the resulting products were analysed using a JEOL-2010F TEM with the assistance of Gatan Digital Micrograph software (Gatan Microscopy Suite 2.0) for image acquisition and processing (FFT, R-FFT, *etc.*).

3. Results and discussion

Raman spectroscopy was used to characterize the formation of WSe_2, $MoSe_2$ and the $MoSe_2/WSe_2$ heterostructures. For the WSe_2 film, one main characteristic peak at 250.5 cm^{-1}, assigned to the E^1_{2g} mode was observed.[21] On the other hand, for the $MoSe_2$ film three characteristic phonon modes appeared in the Raman spectra: a sharp one at low wavenumber ($\sim$242.2 cm^{-1}) associated with the out-of-plane vibration of Se atoms, and two broad ones at higher wavenumber ($\sim$290.1 cm^{-1}), ($\sim$352.0 cm^{-1}) corresponding to the E^1_{2g} and B^1_{2g} modes associated with the in-plane vibration of Mo and Se atoms.[22–24] In the Raman spectrum of the $MoSe_2/WSe_2$ heterostructure, peaks

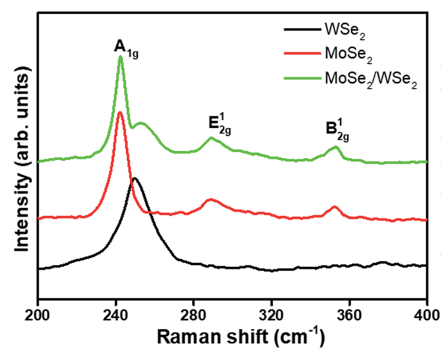

Fig. 2 Raman spectra of WSe_2, $MoSe_2$ and the $MoSe_2/WSe_2$ heterostructure films.

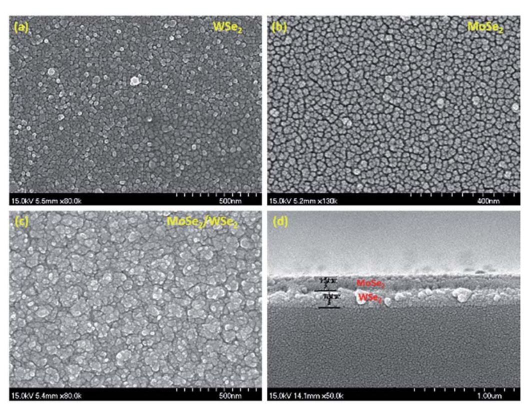

Fig. 3 Top-down and cross-sectional SEM images. Top-down images of (a) WSe_2, (b) $MoSe_2$ and (c) the $MoSe_2/WSe_2$ heterostructure (d) cross-sectional image.

corresponding to both WSe_2 and $MoSe_2$ films appeared. In addition, there was no significant shift of the representative peaks for WSe_2 and $MoSe_2$ in the heterostructure. This supports that there was no serious alloying process of the WSe_2 and $MoSe_2$ encountered in the synthetic procedure, since the alloying process would be accompanied by peak shifts (Fig. 2).[18]

Scanning electron microscope (SEM) images reveal the formation of homogeneous $MoSe_2$ and WSe_2 thin films (Fig. 3a and b). Further, SEM confirms the existence of a dense array of grains for the $MoSe_2/WSe_2$ heterostructure (Fig. 3c). The thicknesses of the $MoSe_2$ and WSe_2 films were $\sim$160 nm and $\sim$140 nm, respectively, estimated from the cross-sectional SEM image (Fig. 3d). The elemental mapping images of W, Mo and Se elements for the $MoSe_2/WSe_2$ heterostructure are provided in the ESI in Fig. S1.† Transmission electron microscopy (TEM) characterization was further performed to analyse the surface of the $MoSe_2/WSe_2$ heterostructure as shown in Fig. 4. The TEM images revealed that the film surface consisted of highly dense layers with a polycrystalline edge-exposed site structure.

X-ray photoelectron spectroscopy (XPS) was applied to examine the binding energies of WSe_2, $MoSe_2$ and the $MoSe_2/WSe_2$ heterostructure (Fig. 5a–d). The complete survey scans of WSe_2 and $MoSe_2$ are provided in Fig. S2.† From the WSe_2 film, the peaks at 32.2 and 34.4 eV were assigned to the doublet W $4f_{7/2}$ and W $4f_{5/2}$ binding energies, respectively and the peak at 38 eV was assigned to W $5p_{3/2}$ binding energy. The Se peaks at 54.7 and 55.1 eV (Fig. 5a and b) were indexed to be Se $3d_{5/2}$ and Se $3d_{3/2}$ respectively.[21,25] For the $MoSe_2$ film, Mo $3d_{3/2}$ and $3d_{5/2}$ core levels peaks were located at 231.1 and 228.0 eV, respectively. The peak of Se around 54.0 eV can be divided into Se $3d_{5/2}$ and Se $3d_{3/2}$ with peak positions at 54.6 and 55.2 eV, respectively[26,27] (Fig. 5c and d). The XPS survey scan of the $MoSe_2/WSe_2$ heterostructure revealed the presence of W, Mo and Se elements (Fig. S3†).

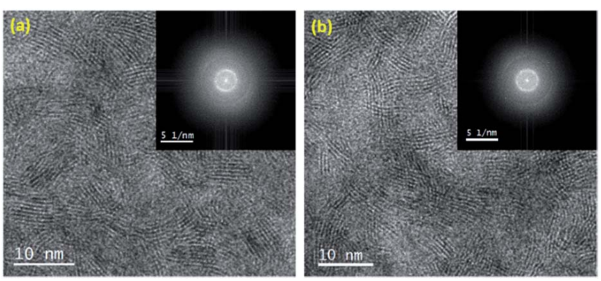

Fig. 4 (a and b) TEM images of the $MoSe_2/WSe_2$ heterostructure.

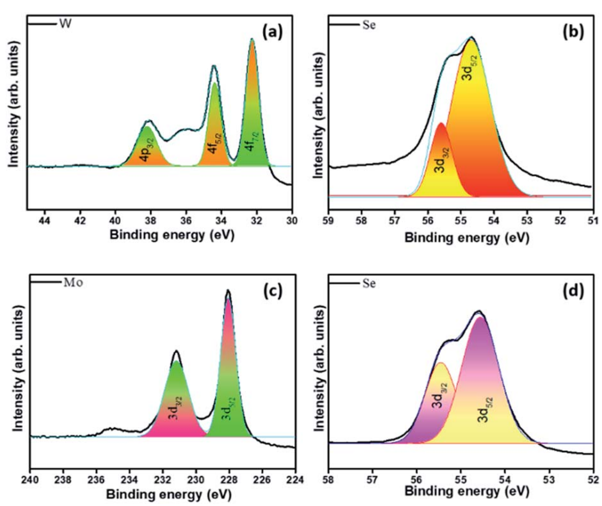

Fig. 5 XPS spectra: (a) W 4f and (b) Se 3d binding energies for WSe_2. (c) Mo 3d, 4f and (d) Se 3d binding energies for $MoSe_2$.

XPS depth profile analysis was performed to investigate the typical $WSe_2/MoSe_2$ heterostructure. A 1 keV Ar ion beam was used for continuous etching of the $WSe_2/MoSe_2$ heterostructure in the direction from top to bottom. Fig. 6a–c show the XPS depth profile spectra for the W, Mo and Se binding energies. The Mo peak intensities were decreased and the W peak intensities were increased with etching time, whereas Se peak intensities were slightly varied due to the presence of Se in both structures. These findings confirm the heterostructure formation without diffusion or alloy formation. The Mo atomic concentration from the top-layer of $MoSe_2$ drastically decreased, although the W atomic concentration from the bottom-layer of WSe_2 linearly increased up to 120 s of etching time as shown in Fig. 6d. The cross sectional SEM image of the heterostructure is also evidence of our dual layered structure.

We characterized the electrical transport properties of WSe_2 and $MoSe_2$ back-gated field effect transistor (FET) devices (Fig. 7a and b). Transfer characteristics of source-drain current (I_{ds}) *versus* back-gate voltage (V_{gs}) were measured for WSe_2 and $MoSe_2$ FETs. The WSe_2 and $MoSe_2$ devices presented p-type and n-type behavior under back-gate biasing (constant bias, $V_{ds} = 1$ V), respectively, similar to the earlier reports by other research group.[22,28] The field-effect mobility was extracted from the slope of $\Delta I_{ds}/\Delta V_{gs}$ fitted to the linear region of the transfer curves using the following equation

$$\mu = \frac{L}{WC_{ox}V_{ds}}\frac{\Delta I_{ds}}{\Delta V_{gs}} \quad (1)$$

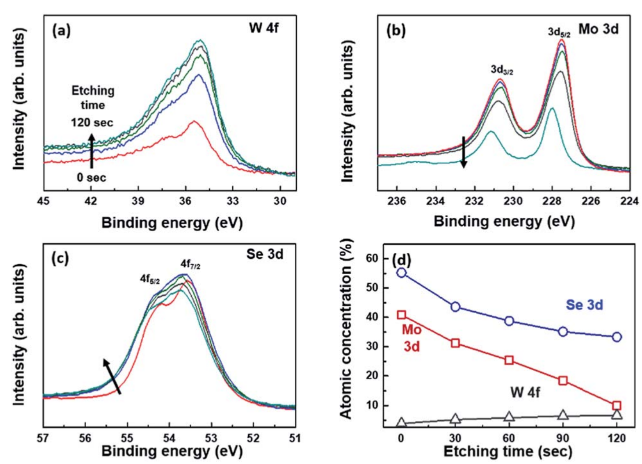

Fig. 6 XPS depth profile spectra of (a) W 4f, (b) Mo 3d, and (c) Se 3d binding energies and (d) their atomic concentration variations in terms of etching time for the $MoSe_2/WSe_2$ heterostructure.

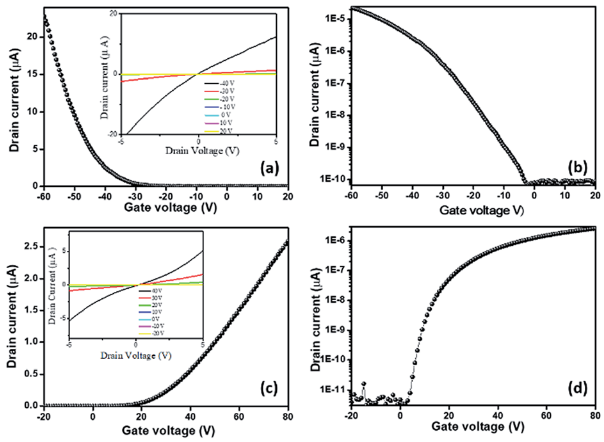

Fig. 7 Electrical output and transfer curves of theWSe$_2$ and MoSe$_2$ devices. (a and b) I_d–V_g of the WSe$_2$ FET at fixed $V_{gs} = 1$ V; I_{ds}–V_{ds} of the WSe$_2$ FET at V_{ds}: 20 V to −40 V (inset). (c and d) I_{ds}–V_{gs} of the MoSe$_2$ FET at $V_{gs} = 1$ V; I_{ds}–V_{ds} of the MoSe$_2$ FET at V_{ds}: 20 V to −40 V (inset).

where W is the width of the channel (10 μm), L is the length of the channel (10 μm), C_{ox} is the capacitance per unit area of the gate dielectric with 300 nm thickness (1.15×10^{-8} F cm^{-1}), V_{ds} is the applied drain voltage and $\Delta I_{ds}/\Delta V_{gs}$ is the slope of the linear part of the transfer plot (I_{ds}–V_{gs}) or the transconductance. The estimated field-effect mobility values of WSe$_2$ and MoSe$_2$ FETs are ∼2.2 cm^2 V^{-1} s^{-1} and ∼15.1 cm^2 V^{-1} s^{-1}, respectively and on/off current ratios are ∼3–6 × 10^5. The linear I_{ds}–V_{ds} characteristics of both WSe$_2$ and MoSe$_2$ devices exhibited good ohmic contacts and there was an absence of significant charge injection barriers. Compared to the subthreshold characteristics, MoSe$_2$ had a better subthreshold swing than WSe$_2$. Electrical properties of the MoSe$_2$/WSe$_2$ heterostructure film were also measured. Voltages were applied to the metal pads of the p-type WSe$_2$ and the n-type MoSe$_2$ with changing back-gate bias. Fig. 8a shows the linear I–V curves of the stacked MoSe$_2$/WSe$_2$ p–n junction at various back-gate voltages. The drain voltage in Fig. 8a is the voltage applied to p-WSe$_2$ with respect to n-MoSe$_2$. Rectifying I–V characteristics were observed from the p–n junction between n-type MoSe$_2$ and p-type WSe$_2$. The current in Schottky barrier diodes can be expressed as

$$I = I_0\left(e^{\frac{qV}{nkT}} - 1\right) \tag{2}$$

where, I_0 is the saturation current, k is the Boltzmann constant, T is the absolute temperature, q is the elementary electric charge, and V is the applied voltage. The saturation current I_0 is expressed as

$$I_0 = AA^*T^2 e^{\frac{-q\Phi_b}{kT}} \tag{3}$$

where, A is the device area, A^* is the effective Richardson constant, and Φ_b is the barrier height. The ideality factor of the Schottky diode is extracted from the slope of the linear region of the ln I–V characteristic and is expressed as

$$n = \left[\frac{q}{kT}\right]\left[\frac{dV}{d(\ln I)}\right] \tag{4}$$

The ideality factor varies with back-gate bias, and is ∼1.5 at a low bias range at $V_{gs} = 40$ V. The forward current is also increased upon increasing the back-gate voltage. The back-gate voltage controls the charge carrier densities of the electrons and holes in n-MoSe$_2$ and p-WSe$_2$. Since the bottom layer is p-type WSe$_2$ and the top layer is n-type MoSe$_2$, it is expected that hole concentration in WSe$_2$ decreases with increasing back-gate bias, while the top n-type MoSe$_2$ is less affected. Since the p–n junction is mainly composed of a vertical n-MoSe$_2$/p-WSe$_2$ junction and partly of a lateral side junction (the vertical junction area is much larger than the lateral side junction), the carrier concentration in the p-WSe$_2$ layer is readily modulated by the back-gate bias, while the electrons in the top MoSe$_2$ is less affected by screening due to the bottom WSe$_2$ layer. Therefore, upon increasing the back-gate bias, the barrier height between WSe$_2$ and MoSe$_2$ decreases, and in turn increases the forward current. Fig. 8b is a plot of logarithmic I *versus* linear V.

The reverse current also increases with increasing back-gate voltage. This is also due to the lowered barrier height between p-WSe$_2$ and n-MoSe$_2$. Fig. 8c shows the rectification ratios of the diode. The rectification ratio is defined as the forward current at 1 V anode bias (the p-WSe$_2$ voltage with respect to the n-MoSe$_2$ voltage) *versus* reverse current at −1 V anode bias. It is observed

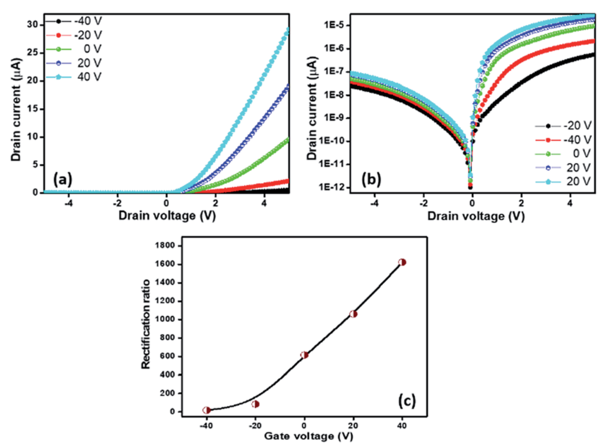

Fig. 8 Linear scale and log scale plots of I–V characteristics of the MoSe$_2$/WSe$_2$ heterojunction (a) linear scale plots of I–V. (b) Log scale I – linear V with different back-gate voltages V_{gs} (c) rectification ratio (I_{ds}@$V_{ds} = 1$ V/I_{ds}@$V_{ds} = -1$ V) as a function of back-gate voltage V_{gs}.

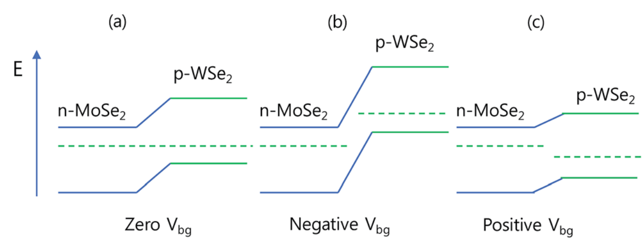

Fig. 9 Energy band diagram of n-MoSe$_2$ and p-WSe$_2$ at (a) 0, (b) negative and (c) positive back-gate voltage.

that the rectification is modulated by the back-gate voltage. The rectification ratio of the diode is increased from ∼20 to ∼1800 as the back-gate bias is varied from −40 V to +40 V as shown in Fig. 8c. This value is much higher than the reported value (∼150) for the TMDC p–n heterostructure (MoS_2/WSe_2) grown by CVD.[18]

The energy band diagram (Fig. 9) reveals the formation of a built-in potential in the heterojunction p-WSe_2/n-$MoSe_2$, in which the conduction band (E_c) of WSe_2 lies above that of $MoSe_2$. The built-in potential is produced due to the formation of a depletion region at the interface. This barrier height is increased at negative gate bias as energy levels in WSe_2 are shifted towards higher energy levels (Fig. 9b). Current is increased when the positive gate bias is applied (Fig. 9c). Positive gate bias leads to a decrease of the electron barrier and the energy levels in WSe_2 shift towards lower energy, which results in the reduction of the barrier between the p- and n-regions and increased the forward current.

4. Conclusions

We fabricated a $MoSe_2$/WSe_2 p–n heterostructure using a sputtering-CVD method. The WSe_2 and $MoSe_2$ back-gated field effect transistors (FETs) exhibited good gate modulation behavior, and high hole and electron mobilities of ∼2.2 and ∼15.1 $cm^2\ V^{-1}\ s^{-1}$, respectively. The fabricated $MoSe_2$/WSe_2 p–n diodes exhibited gate-tunable rectifying *I–V* characteristics. The rectification ratio of the p–n diode is increased with an increase in the gate voltage, and it is increased from ∼18 to ∼1600 as the gate bias is increased from −40 V to +40 V. This is attributed to the fact that the barrier height between p-WSe_2 and n-$MoSe_2$ is lowered due to the back-gate bias. The rectification ratio is much higher than the previously reported value for the TMDC p–n heterostructure (MoS_2/WSe_2) grown by CVD.

Conflicts of interest

There are no conflicts to declare.

Acknowledgements

This research was supported by the Basic Science Research Program and the Nano Material Technology Development Program through the National Research Foundation of Korea (NRF), and was funded by the Ministry of Education (2010-0020207, NRF-2016R1D1A1B01015047, 2018044021), and the Ministry of Science, ICT and Future Planning (NRF-2015M3A7B7045194, 2016M3A7B4909942).

Notes and references

1 G.-B. Liu, D. Xiao, Y. Yao, X. Xu and W. Yao, *Chem. Soc. Rev.*, 2015, **44**, 2643–2663.
2 M. Chhowalla, H. S. Shin, G. Eda, L.-J. Li, K. P. Loh and H. Zhang, *Nat. Chem.*, 2013, **5**, 263–275.
3 Q. H. Wang, K. Kalantar-Zadeh, A. Kis, J. N. Coleman and M. S. Strano, *Nat. Nanotechnol.*, 2012, **7**, 699–712.
4 L. Xie, *Nanoscale*, 2015, **7**, 18392–18401.
5 A. Ramasubramaniam, *Phys. Rev. B*, 2012, **86**, 115409.
6 W. Zhao, Z. Ghorannevis, L. Chu, M. Toh, C. Kloc, P.-H. Tan and G. Eda, *ACS Nano*, 2013, **7**, 791–797.
7 B. Radisavljevic, A. Radenovic, J. Brivio, I. V. Giacometti and A. Kis, *Nat. Nanotechnol.*, 2011, **6**, 147–150.
8 S. Kim, A. Konar, W.-S. Hwang, J. H. Lee, J. Lee, J. Yang, C. Jung, H. Kim, J.-B. Yoo and J.-Y. Choi, *Nat. Commun.*, 2012, **3**, 1011, DOI: 10.1038/ncomms2018.
9 H. Fang, M. Tosun, G. Seol, T. C. Chang, K. Takei, J. Guo and A. Javey, *Nano Lett.*, 2013, **13**, 1991–1995.
10 R. Vargas-Bernal, in *Two-dimensional Materials-Synthesis, Characterization and Potential Applications*, InTech, 2016: DOI: 10.5772/63916.
11 B. Radisavljevic, M. B. Whitwick and A. Kis, *ACS Nano*, 2011, **5**, 9934–9938.
12 L. Ye, H. Li, Z. Chen and J. Xu, *ACS Photonics*, 2016, **3**, 692–699.
13 C.-H. Lee, G.-H. Lee, A. M. Van Der Zande, W. Chen, Y. Li, M. Han, X. Cui, G. Arefe, C. Nuckolls and T. F. Heinz, *Nat. Nanotechnol.*, 2014, **9**, 676–681.
14 Y. Yi, C. Wu, H. Liu, J. Zeng, H. He and J. Wang, *Nanoscale*, 2015, **7**, 15711–15718.
15 K. M. McCreary, A. T. Hanbicki, J. T. Robinson, E. Cobas, J. C. Culbertson, A. L. Friedman, G. G. Jernigan and B. T. Jonker, *Adv. Funct. Mater.*, 2014, **24**, 6449–6454.
16 Y. Gong, J. Lin, X. Wang, G. Shi, S. Lei, Z. Lin, X. Zou, G. Ye, R. Vajtai and B. I. Yakobson, *Nat. Mater.*, 2014, **13**, 1135–1142.
17 M. Okada, T. Sawazaki, K. Watanabe, T. Taniguch, H. Hibino, H. Shinohara and R. Kitaura, *ACS Nano*, 2014, **8**, 8273–8277.
18 J. H. Yu, H. R. Lee, S. S. Hong, D. Kong, H.-W. Lee, H. Wang, F. Xiong, S. Wang and Y. Cui, *Nano Lett.*, 2015, **15**, 1031–1035.
19 S. Hussain, M. A. Shehzad, D. Vikraman, M. F. Khan, J. Singh, D.-C. Choi, Y. Seo, J. Eom, W.-G. Lee and J. Jung, *Nanoscale*, 2016, **8**, 4340–4347.
20 S. Hussain, M. F. Khan, M. A. Shehzad, D. Vikraman, M. Z. Iqbal, D.-C. Choi, W. Song, K.-S. An, Y. Seo and J. Eom, *J. Mater. Chem. C*, 2016, **4**, 7846–7852.
21 S. Li, S. Wang, D.-M. Tang, W. Zhao, H. Xu, L. Chu, Y. Bando, D. Golberg and G. Eda, *Appl. Mater. Today*, 2015, **1**, 60–66.
22 X. Wang, Y. Gong, G. Shi, W. L. Chow, K. Keyshar, G. Ye, R. Vajtai, J. Lou, Z. Liu and E. Ringe, *ACS Nano*, 2014, **8**, 5125–5131.
23 X. Lu, M. I. B. Utama, J. Lin, X. Gong, J. Zhang, Y. Zhao, S. T. Pantelides, J. Wang, Z. Dong and Z. Liu, *Nano Lett.*, 2014, **14**, 2419–2425.
24 P. Tonndorf, R. Schmidt, P. Böttger, X. Zhang, J. Börner, A. Liebig, M. Albrecht, C. Kloc, O. Gordan and D. R. Zahn, *Opt. Express*, 2013, **21**, 4908–4916.
25 J. Chen, B. Liu, Y. Liu, W. Tang, C. T. Nai, L. Li, J. Zheng, L. Gao, Y. Zheng and H. S. Shin, *Adv. Mater.*, 2015, **27**, 6722–6727.
26 G. W. Shim, K. Yoo, S.-B. Seo, J. Shin, D. Y. Jung, I.-S. Kang, C. W. Ahn, B. J. Cho and S.-Y. Choi, *ACS Nano*, 2014, **8**, 6655–6662.
27 A. Wa'el and A. Nelson, *J. Mater. Sci.*, 2005, **40**, 2679–2681.
28 H. Zhou, C. Wang, J. C. Shaw, R. Cheng, Y. Chen, X. Huang, Y. Liu, N. O. Weiss, Z. Lin and Y. Huang, *Nano Lett.*, 2015, **15**, 709–713.

